



Title	Influence of topography on temperature variations in the tropical tropopause layer
Author(s)	Kubokawa, Hiroyasu; Satoh, Masaki; Suzuki, Junko; Fujiwara, Masatomo
Citation	Journal of geophysical research atmospheres, 121(19), 11556-11574 https://doi.org/10.1002/2016JD025569
Issue Date	2016-10
Doc URL	http://hdl.handle.net/2115/63930
Rights(URL)	http://creativecommons.org/licenses/by-nc-nd/4.0/
Type	article
File Information	Kubokawa_et_al-2016-Journal_of_Geophysical_Research__Atmospheres.pdf



[Instructions for use](#)



RESEARCH ARTICLE

10.1002/2016JD025569

Key Points:

- Mountainous regions are favorable locations for large temperature variations in the TTL
- Superposition of gravity waves and Kelvin waves has the potential to produce the coldest region
- Terrain-following coordinate system may produce unrealistic temperature variations in the TTL

Correspondence to:

H. Kubokawa,
kubok@aori.u-tokyo.ac.jp

Citation:

Kubokawa, H., M. Satoh, J. Suzuki, and M. Fujiwara (2016), Influence of topography on temperature variations in the tropical tropopause layer, *J. Geophys. Res. Atmos.*, 121, 11,556–11,574, doi:10.1002/2016JD025569.

Received 29 JUN 2016

Accepted 25 SEP 2016

Accepted article online 28 SEP 2016

Published online 12 OCT 2016

Influence of topography on temperature variations in the tropical tropopause layer

Hiroyasu Kubokawa¹, Masaki Satoh^{1,2}, Junko Suzuki², and Masatomo Fujiwara³

¹Atmosphere Ocean Research Institute, The University of Tokyo, Kashiwa, Japan, ²Japan Agency for Marine-Earth Science and Technology, Yokosuka, Japan, ³Faculty of Environmental Earth Science, Hokkaido University, Sapporo, Japan

Abstract Temperature variations in the tropical tropopause layer (TTL) play an important role in dehydration in the upper troposphere and lower stratosphere. Equatorial Kelvin waves associated with the Madden-Julian Oscillation (MJO) are known to induce remarkable temperature variations in the TTL. In this study, the influence of topography on temperature variations in the TTL is investigated by using radiosonde data, satellite data, reanalysis data, and numerically simulated data. When MJO convection passes over the radiosonde sites, temperature variations near mountainous regions are larger than those measured in regions of lower elevation. The difference in temperature amplitude reaches ~1–2 K. Large temperature variations over mountainous regions were also found in other data sets. Numerically simulated data from the Nonhydrostatic Icosahedral Atmospheric Model (NICAM) are also used to investigate the temperature variations in the TTL. The results show that the temperature variations associated with Kelvin waves become large over mountainous regions. A sensitivity test using the stretched version of NICAM gave two important results: (i) the height of mountains affects the magnitude of the temperature variations in the TTL, and (ii) the terrain-following coordinate system used in the model produces the artificially high-temperature variation in the TTL. When Kelvin waves pass over mountainous regions, topographic gravity waves are excited and superimposed on the Kelvin waves, thereby producing large temperature variations over these regions. The mountainous region of the Indonesian Maritime Continent is a favorable location for large temperature variations in the TTL.

1. Introduction

The tropical tropopause layer (TTL) is the coldest region in the troposphere. Because of the cold temperature, the saturated water vapor mixing ratio becomes low in the TTL. When air enters the stratosphere from the troposphere through the TTL, substantial dehydration occurs. As stratospheric ozone is affected by the amount of water vapor entering the stratosphere [e.g., Holton *et al.*, 1995; Kley *et al.*, 2000; Fueglistaler *et al.*, 2009], temperature variations in the TTL are thought to be an important factor controlling the amount of stratospheric ozone.

Observations of the cold point (CP) temperature in the TTL show that the tropopause temperature in the Northern Hemisphere winter is colder than in the Northern Hemisphere summer [e.g., Newell and Gould-Stewart, 1981; Holton *et al.*, 1995]. The amplitude of the seasonal cycle of CP temperature reaches ~2 K [Seidel *et al.*, 2001]. This seasonal temperature difference leads to a clear seasonal difference in the amount of water vapor entering the stratosphere. The tropical lower stratospheric water vapor mixing ratio in the Northern (Southern) Hemisphere winter is less (greater) than 3 ppmv (4 ppmv) [e.g., Mote *et al.*, 1996; Fujiwara *et al.*, 2010].

In the Northern Hemisphere winter, the coldest region of the TTL is found over the western Pacific, where the tropopause temperature reaches ~191 K, which is ~2 K colder than in other tropical regions [Seidel *et al.*, 2001]. This temperature difference plays an important role in controlling stratospheric humidity [e.g., Holton and Gettelman, 2001; Inai *et al.*, 2013].

The TTL temperature is also modulated by equatorial waves with a time scale shorter than the seasonal cycle. Equatorial Kelvin waves cause tropopause temperature variations with a period of 7–14 days [e.g., Tsuda *et al.*, 1994; Fujiwara *et al.*, 1998]. The amplitude of the temperature variations reaches ~4 K [Tsuda *et al.*, 1994], and the cold phase of Kelvin waves causes local dehydration [Immler *et al.*, 2008]. Gravity waves also modulate the tropopause temperature. Pfister *et al.* [1993] first discussed temperature variations associated with gravity waves by using observations from the Stratosphere-Troposphere Exchange Project. They showed that gravity

©2016. The Authors.

This is an open access article under the terms of the Creative Commons Attribution-NonCommercial-NoDerivs License, which permits use and distribution in any medium, provided the original work is properly cited, the use is non-commercial and no modifications or adaptations are made.

waves with a period of 5–6 h introduce modulation of the tropopause temperature with an amplitude of 2.5 K. Kubokawa *et al.* [2012] used output data from the Nonhydrostatic ICosahedral Atmospheric Model (NICAM) simulations to demonstrate that the temperature variations in the TTL are associated with gravity waves. They showed that gravity waves generated by tropical cyclones induce temperature variations with an amplitude of 1.9 K, extending 1000 km from the tropical cyclone.

Kubokawa *et al.* [2010] also used NICAM simulations and showed that a large-amplitude gravity wave with a zonal scale of 600 km is superimposed on the cold phase of Kelvin waves. The superposition of the waves produces the coldest regions in the TTL. Kubokawa *et al.* [2010] reported that the gravity waves are generated by deep convection. Suzuki *et al.* [2013] observed variability in cirrus clouds using radiosonde data and a shipborne high-spectral-resolution lidar system, revealing that cirrus cloud variability is associated with inertia-gravity waves and equatorial Kelvin waves (both with a period of ~4 days), and equatorial Kelvin waves (period of ~16 days). The superposition of different waves is an important factor in generating the extremely cold region in the TTL.

In general, the generation of gravity waves in the equatorial region is thought to be related to deep convection or mountains [e.g., Satomura and Bougeault, 1994; Zhang *et al.*, 2013, 2014]. Over mountainous regions, various waves from small to large scales may coexist. We therefore investigate the influence of topography on temperature variations in the TTL. In our previous study [i.e., Kubokawa *et al.*, 2012], we found that temperature variations over mountainous regions had amplitudes twice as large as those over the ocean. This temperature difference may be a model artifact. There is still a possibility that the temperatures become colder over the mountainous regions even in the real atmosphere. Gravity wave drag is an important control on atmospheric circulation. The orientation of mountain ranges is also important for momentum transport [Satomura, 1996]. As horizontal resolution becomes higher, the scale or orientation of mountain ranges also becomes important. All these factors mean that we should investigate the characteristics of gravity waves near mountainous regions.

We focus on the differences in temperature variations between the mountainous region in the Indonesian Maritime Continent and the western Pacific Ocean. We use radiosonde data obtained from the Cooperative Indian Ocean experiment on intraseasonal variability in the Year 2011 (CINDY) and the Dynamics of the Madden-Julian Oscillation (MJO) (DYNAMO) observational campaign [e.g., Yoneyama *et al.*, 2013]. We also analyze Constellation Observing System for Meteorology, Ionosphere and Climate (COSMIC) satellite data and four types of reanalysis data. We use NICAM [Tomita and Satoh, 2004; Satoh *et al.*, 2008, 2014] to investigate the sensitivity of temperature variability to model configuration and the mechanisms generating these large temperature variations. The model has a horizontal resolution of ~7 km, which enables us to investigate the different characteristics of temperature variations over mountainous regions and the ocean.

The remainder of this paper is organized as follows. We describe the methodology and details of each data set in section 2. Section 3 presents the temperature variations obtained from radiosonde data, satellite data, reanalysis data, and NICAM simulations. In section 4, we use the stretched version of NICAM [Tomita, 2008b] to show the role of topography in the temperature variations in the TTL, and we discuss the gravity wave characteristics simulated by the model. Details of the stretched version of NICAM (Stretch-NICAM) are also discussed in section 4. Finally, our conclusions are provided in section 5.

2. Data

2.1. Observational Data

We use radiosonde data obtained during the CINDY/DYNAMO field campaign at Singapore (103.80°E, 1.33°N, 14 m), Padang (100.35°E, 0.88°S, 2 m), Medan (98.40°E, 3.33°N, 27 m), Makassar (119.31°E, 5.03°S, 12 m), Palu (119.90°E, 0.91°S, 84 m), and Male (73.53°E, 4.19°N, 2 m). The first three stations (Singapore, Padang, and Medan) are located near mountainous regions in the Indonesian Maritime Continent, while the other stations (Makassar, Palu, and Male) are located on plains. We analyze the data from 30 September 2011 to 31 March 2012 at all stations except Male. At Male, we use the data from 30 September 2011 to 31 December 2011. Only the Male data are processed at 5 hPa intervals. At other observatories, data are obtained every second (corresponding to about 5 m in the vertical). We also use

Table 1. Details of Model and Reanalysis Data

Model Name	Data	H-Space (Offered)		Note
		Model Resolution		
NICAM MJO experiment	15 December 2006 to 15 January 2007	0.07° (7 km) ~7 km 1.5° ~80 km 1.25° 0.5° × 0.66°, or ~50 km 0.5° ~38 km		
ERA-Interim				To compare the model grid resolution
MERRA				
NCEP-CFSR				
ECMWF-YOTC	December (2008 and 2009) January (2009 and 2010) February (2009 and 2010)	0.125° ~25 km		To show results obtained by using a high horizontal resolution
Stretch-NICAM glevel 7	1 June 2012 to 5 June 2012	0.07° (7 km) ~7 km		To investigate the influence of topography and the vertical grid scheme

the data obtained from the observing ship, R/V *Roger Revelle*. We analyze the data from 12 September 2011 to 30 January 2012, when R/V *Roger Revelle* cruised between 10°S and 10°N. We vertically interpolated all the data at 100 m intervals. The uncertainty in these temperature measurements is 0.5 K.

The GPS radio occultation (RO) temperature profiles obtained from COSMIC data [Anthes et al., 2008] during the Northern Hemisphere winter, January (2007–2010), February (2007–2009), and December (2006–2009), are also analyzed. In the data period from 2006 to 2009, ~1500–2000 temperature profiles are available per day, while ~1000 temperature profiles are available per day after 2010. These data have 100 m vertical resolution from the surface to levels above 30 km. Since the GPS RO technique is influenced by the water vapor amount in the lower troposphere, we only analyze the data above 16 km altitude where the water vapor amount is low. The GPS RO data were downloaded from the COSMIC Data Analysis and Archive Center website (<http://cosmic-io.cosmic.ucar.edu/cdaac/index.html>). The horizontal distribution of average temperature is shown in section 3.1. We calculated the average field used for Figures 3a and 3b by the following two steps. (1) We sampled the temperature and location information at altitudes of 16.1 and 16.9 km during the period between 16 December 2006 and 15 January 2007 (this period corresponds to that of the NICAM MJO experiment discussed in section 2.3). (2) We then averaged these temperature data over each 2.5° × 2.5° bin in the tropics (30°S–30°N). Note that there are on average three data points per bin at the equator and six data points per bin in the subtropics. For the calculation of the standard deviation of temperature (Figure 3c), we used 1° × 1° bins and data from four northern hemisphere winters, i.e., during December (2006–2009), January (2007–2010), and February (2007–2009). In this case, there are on average 10 (15) data points per bin at the equator (in the subtropics).

2.2. Reanalysis Data

Four reanalysis data sets are analyzed: (1) the European Centre for Medium-Range Weather Forecasts (ECMWF) Interim Re-analysis (ERA-Interim) [Dee et al., 2011], (2) Modern Era Retrospective-analysis for Research and Applications (MERRA) [Rienecker et al., 2011], (3) National Centers for Environmental Prediction-Climate Forecast System Reanalysis (NCEP-CFSR) [Saha et al., 2010], and (4) ECMWF Year of Tropical Convection (ECMWF-YOTC) [e.g., Moncrieff et al., 2012]. The horizontal spacing of these data is 1.5°, 1.25°, 0.5°, and 0.125°, respectively. The data period for the first three data sets (1)–(3) is from 16 December 2006 to 15 January 2007, the same as for the NICAM MJO experiment discussed below in section 2.3. For the ECMWF-YOTC data (4), we use December (2008 and 2009), January (2009 and 2010), and February (2009 and 2010) data because of the limited period available. The data information listed above is summarized in Table 1. In these data periods, GPS RO data are assimilated into NCEP-CFSR and ECMWF-YOTC.

2.3. Numerically Simulated Data

We use experimental data from the NICAM simulation run under the atmospheric conditions of 15 December 2006 to 15 January 2007 by Miura et al. [2007]. This data set was also analyzed by Kubokawa et al. [2012]. This experiment captured the characteristics of the Madden-Julian Oscillation (MJO) [Madden and Julian, 1994],

such as the eastward propagation of large-scale organized clouds with a horizontal scale of several thousand kilometers. We refer to this experiment as the NICAM MJO experiment. NICAM uses an icosahedral grid with a nonhydrostatic system and does not use a cumulus parameterization scheme. The horizontal spacing was set as 3.5 km and 7 km in *Miura et al.* [2007]. We use only 7 km grid data because its integration period extends to ~1 month, while the 3.5 km experiment was only run for a week. The number of vertical levels was set as 40 with the model top at 38 km and a vertical spacing of 1.4 km in the upper troposphere. The initial conditions of the experiment are from the National Centers for Environmental Prediction (NCEP) Global Tropospheric Analysis data. There was no nudging of the atmospheric data during the integration. The sea surface temperature (SST) condition was given by the weekly mean data of the Reynolds SST data set. The vertical spacing of this experiment might appear a little coarse, but it was found that the simulated TTL temperature variation, such as the phase speed associated with Kelvin waves, corresponded closely to the reanalysis data [*Kubokawa et al.*, 2012]. The average features, the characteristics of deep convection, and the influence of the waves on the TTL temperature variation were also discussed in *Kubokawa et al.* [2012]. In section 4, we also use the Stretch-NICAM [*Tomita*, 2008b] to investigate the sensitivity of the variability in tropopause temperature to the model configuration. The details of the experimental setup for Stretch-NICAM are described in section 4. ERA-Interim and the National Oceanic and Atmospheric Administration (NOAA) outgoing longwave radiation (OLR) data are used to evaluate the reproducibility of the Stretch-NICAM simulation. In section 3.1, we also use these two data sets to evaluate large-scale disturbances. The GTOPO30 data are used as topography in the Stretch-NICAM simulation. This data set was developed by the U.S. Geological Survey's Center for Earth Resources Observation and Science (<https://lta.cr.usgs.gov/GTOPO30>). It has a horizontal spacing of about 1 km.

3. Results

3.1. Observational Data (CINDY/DYNAMO Field Campaign Radiosonde Data and COSMIC Satellite Data)

First, we discuss the temperature variation by using radiosonde data observed during the CINDY/DYNAMO field campaign (see Figure 1). In the CINDY/DYNAMO observational campaign, there were 19 observatories between 30°E and 140°E, 15°S and 15°N (see Figure 2). Because we focus on the influence of topography, we use the three sites near the mountainous region and three observatories away from the mountainous region. Here we regard the sites around 100°E (Singapore, Indonesia Padang, and Indonesia Madan) as near the mountainous region, and 120°E (Indonesia Makassar and Indonesia Palu) and 75°E (Male) and R/V *Roger Revelle* as observatories away from the mountainous region. Here we show the results at 16.1 km height. The results at other heights, such as 16.9 km (corresponding to the cold point tropopause in the NICAM simulation, as discussed in section 4 [see *Kubokawa et al.*, 2012, Figure 2]), show similar amplitudes in temperature variations. At all the observatories, low temperatures lasting for about 2 weeks are seen in the second half of almost every month. In ERA-Interim reanalysis data, this low temperature is associated with the eastward propagating convective system of an MJO (not shown). During the CINDY/DYNAMO observational campaign, standard deviations of temperature at Singapore, Padang, Medan, Makassar, Palu, and Male are 2.82, 3.07, 2.82, 2.40, 2.60, and 2.27 K (see Figure 1h), respectively. Since there is a lot of missing data from R/V *Roger Revelle* compared with other observatories, we do not calculate the standard deviation for the ship data. As stated in section 2, the campaign period for Male is shorter than at the other observatories. We found that the temperature variations (amplitude) associated with the MJO convective system are larger at the observatories near the mountainous region (100°E) than at those farther away. We focus on the period between 30 December 2011 and 10 January 2012, when the coolest (warmest) temperature reaches 188–190 K (200–201 K) near the mountainous region, while in the observatories away from the mountainous region (around 120°E), the coolest (warmest) temperature reaches 190 K (199–200 K). The amplitude of the temperature variations becomes larger, reaching ~1–2 K near the mountainous region; this amplitude is observed at Singapore and Padang. Note that the temperature variation at Palu in the first half of October is almost as large as at Singapore or Padang. Similarly, the temperature variation measured by the R/V *Roger Revelle* (Figure 1g) between 30 November and 5 December shows a slightly smaller amplitude than that measured at Singapore or Padang, probably because of the superposition of small-scale disturbances [e.g., *Kubokawa et al.*, 2010; *Suzuki et al.*, 2013].

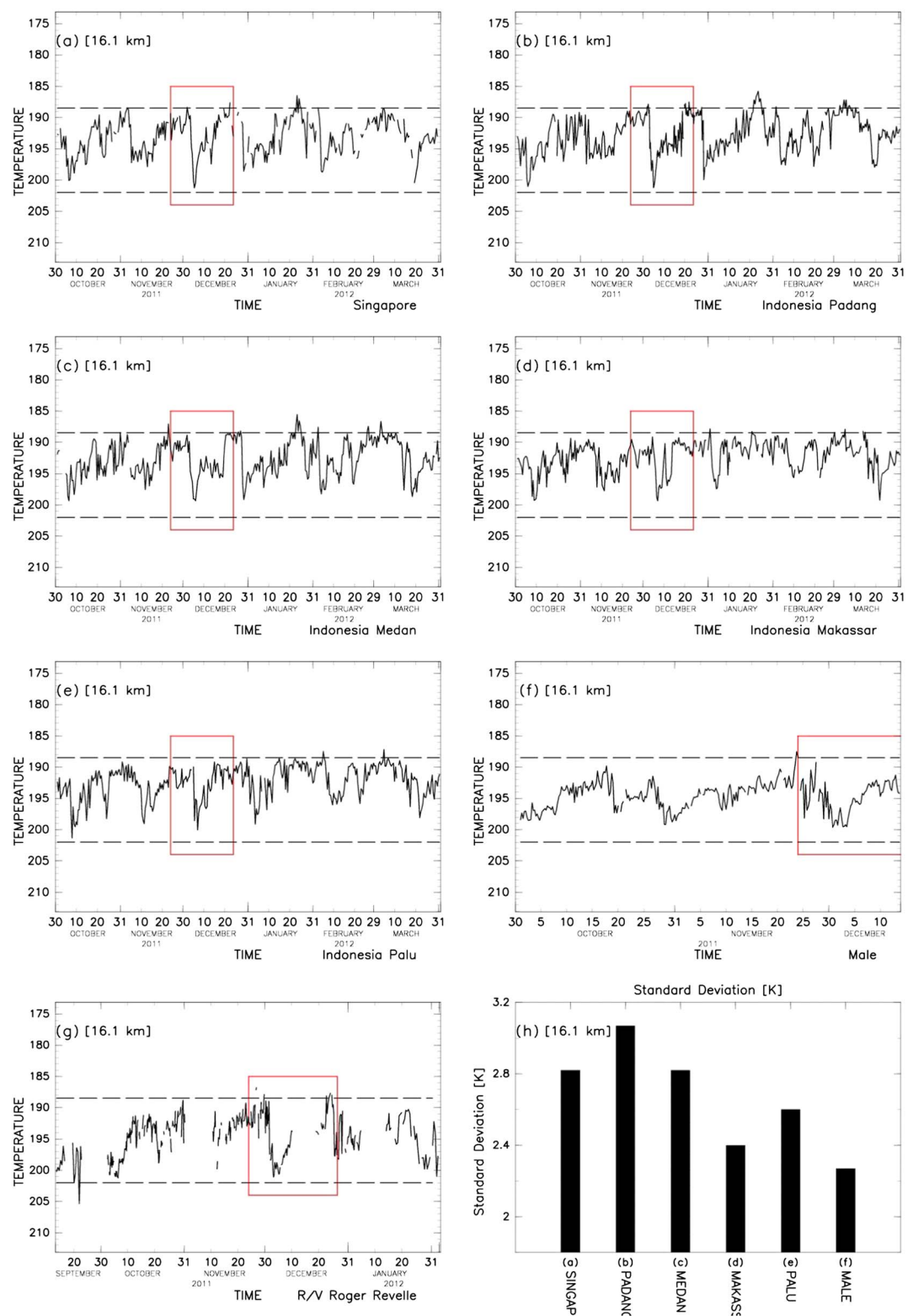


Figure 1. Temperature variation at 16.1 km at (a) Singapore, (b) Padang, (c) Medan, (d) Makassar, (e) Palu, (f) Male, and (g) R/V Roger Revelle. (h) Standard deviation of temperature variation at observatories (a) to (f). The dashed lines in Figures 1a–1g correspond to temperatures of 191.5 K and 202 K.

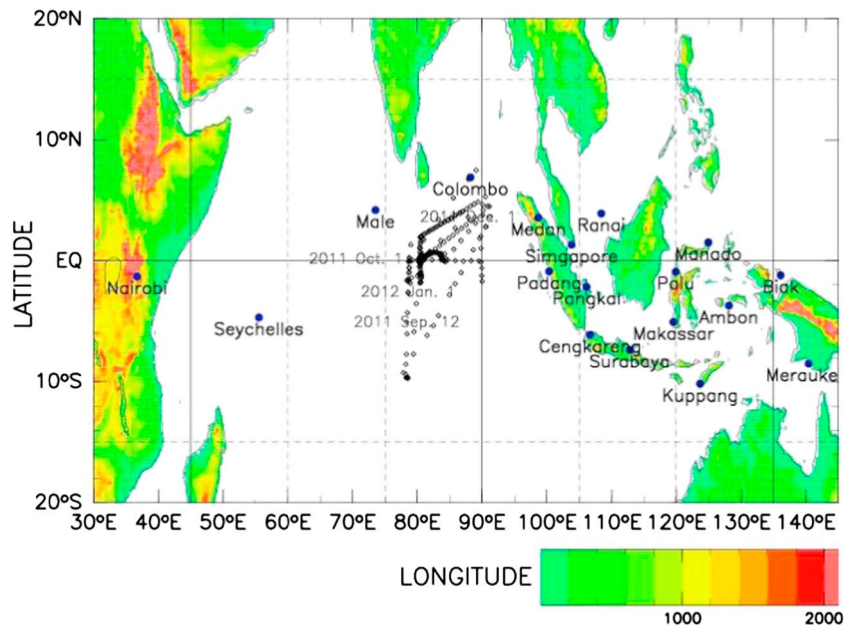


Figure 2. Locations of the observatories involved in the CINDY/DYNAMO field campaign. The small dots indicate observations from the *R/V Roger Revelle*. The position of the *R/V Roger Revelle* is shown as small dots. The color shading indicates height of topography (m).

Next, we discuss the result from COSMIC satellite data. Figures 3a and 3b show the horizontal distribution of temperature at 16.1 km and 16.9 km averaged over the time period for the NICAM MJO experiment, as stated in section 2.1. Figures 3a and 3b show that the cold regions are found over the western Pacific, the American continent, and the African continent. We found that the temperature derived from reanalysis data (Figure 4) over the continent is 2 K colder than that from COSMIC satellite data. Comparing Figure 4 (from the NICAM MJO experiment data at 16.9 km and from reanalysis data at 100 hPa or 16.1 km) with Figure 3 (from COSMIC data at 16.9 km and 16.1 km), we find that the NICAM MJO experiment data showed tropical tropopause temperatures 2 K colder than the reanalysis data, while the reanalysis data generally showed temperatures 2 K colder than COSMIC data. However, the horizontal anomaly patterns are quite similar among the three data sets. Figure 3c also shows the longitudinal distribution of the standard deviation of temperature at 16.1 km and 16.9 km. Here we use the data between 1°N and 2°N. We selected this latitudinal zone because radiosonde sites (see Figure 2) are located within this region. We found that longitudinal variations are very similar between these two levels. A high standard deviation is found around 100°E, 110°E, and 115°E. These longitudes correspond to the mountainous regions (see Figure 5d). Although the number of samples is small in each bin, the standard deviation at these bins (longitudes) is statistically significant (90% significance level, *F*-distribution). Here the significance level is determined at each bin (longitude). If the standard deviation at a given bin is sufficiently large compared with that of the next bin (longitude), it is deemed to be statistically significant. If we only use the period between December 2006 and January 2007 (corresponding to the MJO experiment period), although we find clear large temperature variations around the mountainous region, there are many gaps in the data (not shown). If we use a $2.5^\circ \times 2.5^\circ$ grid bin so that the number of samples increases, we do not find this large temperature variation near the mountainous region. This result indicates that the scale of the phenomenon is smaller than $2.5^\circ \times 2.5^\circ$.

3.2. Reanalysis Data

We examine temperature variations in the TTL in the four reanalysis data sets. First, we show the average field from each reanalysis. Figure 4 shows the horizontal distribution of average temperature at 100 hPa (around the tropopause). These figures, except for the ECMWF-YOTC data, were averaged between 16 December 2006 and 15 January 2007 in order to directly compare them with the results from the NICAM MJO experiment discussed in the next section. For the ECMWF-YOTC data, only selected periods are available, so we averaged temperatures for the following winter seasons: December (2008

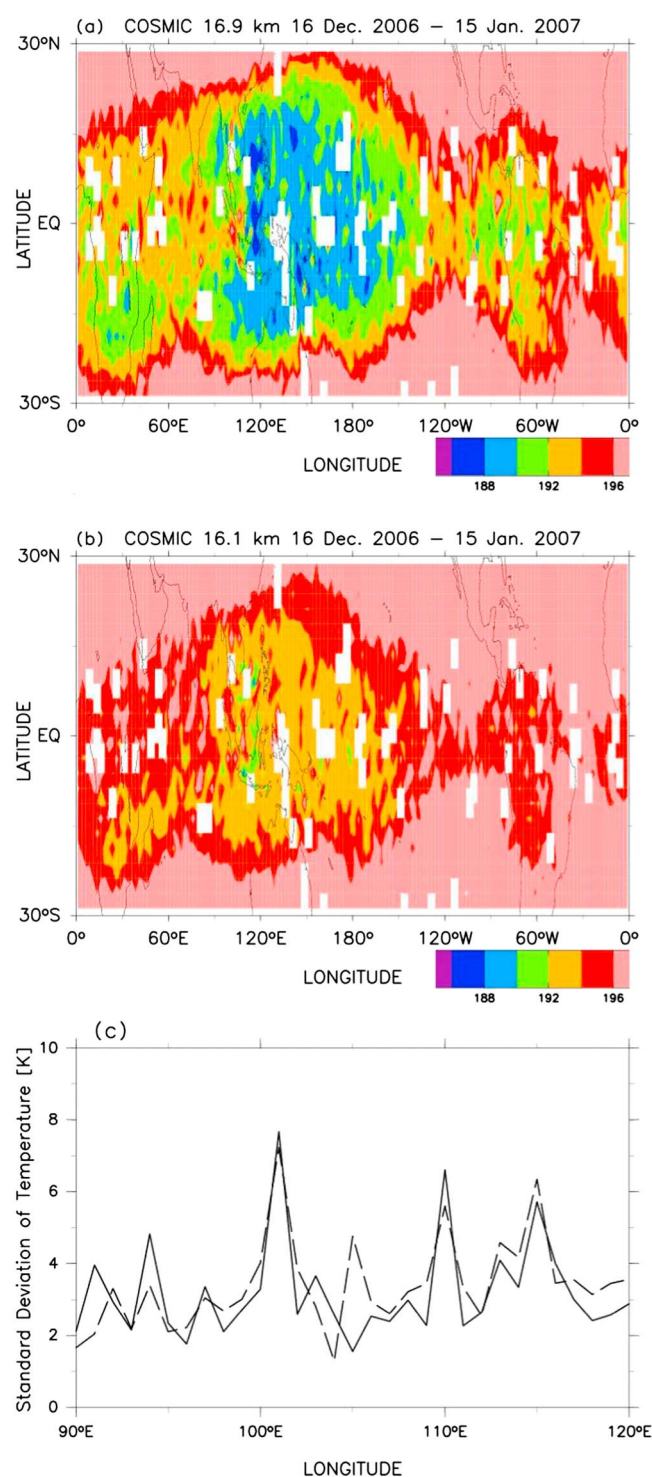


Figure 3. Horizontal distribution of the average temperature from COSMIC data at (a) 16.9 km and (b) 16.1 km during the period of the NICAM MJO experiment (16 December 2006 to 15 January 2007). (c) Longitudinal distribution of the standard deviation of temperature at 16.1 km (black line) and 16.9 km (dashed line) between 1°N and 2°N, calculated from COSMIC data during three Northern Hemisphere winters: December (2006–2009), January (2007–2010), and February (2007–2009).

and 2009), January (2009 and 2010), and February (2009 and 2010). We found that an area of relatively low temperatures over the western Pacific region formed a horseshoe shape pattern [Highwood and Hoskins, 1998; Nishimoto and Shiotani, 2012]. The horizontal distribution of vertically coldest temperatures (less than 190 K) was similar in the four reanalysis data sets. However, the temperature over the western Pacific region of the NICAM MJO experiment (Figure 4a) is ~2 K colder than in the reanalysis data (Figures 4b–4e). It should be noted that these two levels (i.e., the heights of the NICAM MJO experiment (16.9 km) and the reanalysis data (100 hPa)) are different.

Figure 5 shows the standard deviation of temperature near 1°N. Over the western Pacific region, there are three high topography regions between 1°N and 2°N, around 100°E (Sumatra), 110°E, and 115°E (Kalimantan) (see Figure 5d). Note that the selected latitudes for each reanalysis data set are slightly different because the horizontal spacing is different between the data sets. The standard deviations of temperature have a similar structure in all data sets. At around 94°E and between 104°E and 116°E, higher values of the standard deviation are found. In contrast, lower values are seen around 100°E and east of 115°E. The higher values between 104°E and 116°E correspond to the mountainous region around 114°E as shown by Figure 5d. However, there were smaller standard deviations for another mountain range around 100°E. Thus, temperature variations over the mountainous region are not necessarily larger in the reanalysis data. However, temperature variations over the mountainous region (between 110°E and 116°E) increase with increasing horizontal resolution of the reanalysis data (that is, the resolution of the numerical model used for the reanalysis data).

Next, we discuss the results from the higher horizontal resolution ECMWF-YOTC data (0.125°). As discussed in

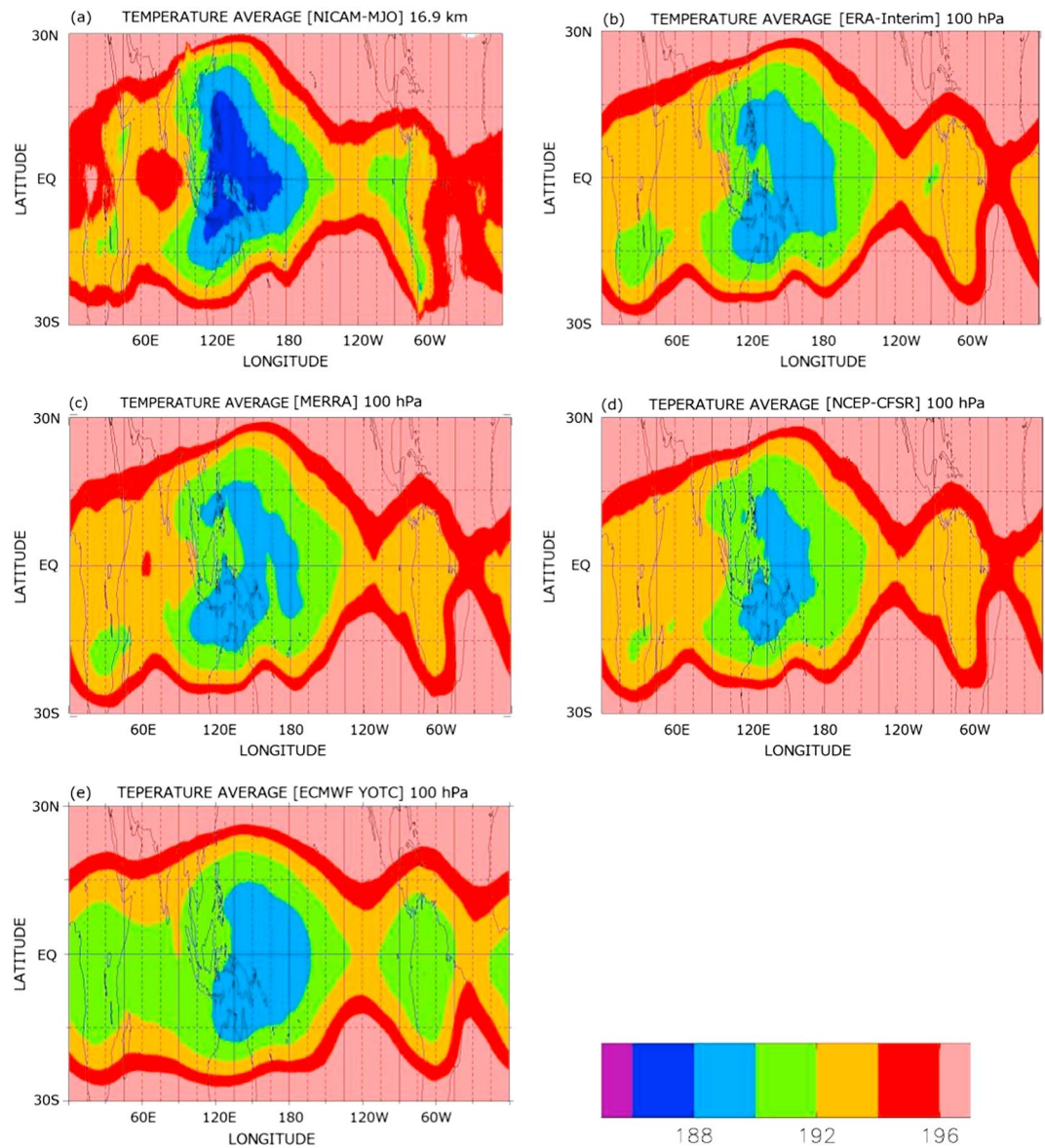


Figure 4. Horizontal distributions of the average temperature (from the (a) NICAM MJO experiment at 16.9 km during the period between 16 December 2006 and 15 January 2007 and from the reanalyses (b) ERA-Interim, (c) MERRA, and (d) NCEP-CFSR during the same period. (e) Horizontal distributions of the average temperature at 100 hPa during the three winter seasons: December (2008 and 2009), January (2009 and 2010), and February (2009 and 2010).

section 2, the data period differs from the other reanalysis data. We focus on the period between 1 December 2009 and 28 February 2010, during which a clear eastward propagating signal is evident (Figure 6a). In December 2009, two cold anomaly events were seen between 90°E and 120°E; the first event was around 12 December, and the second was around 25 December. Similarly, we found two warm anomaly events in the same longitudinal range; the first warm event was around 1 December, and the second was around 20 December. These cold and warm anomalies were eastward propagating signals and are considered to be Kelvin waves; they possess several characteristics of Kelvin waves discussed in Parker [1973] (not shown). We focus on the temperature variations associated with these Kelvin waves.

Locally warmer temperatures were evident between 110°E and 120°E, for example, on 20 December 2009, 10 January 2010, and 20 January 2010 (see Figure 6a). Figures 6b and 6c show the temperature variations at 115°E and 120°E. In December 2009, we found a clear temperature variation with wave-number-one structure (indicating Kelvin waves) [Kubokawa et al., 2012]. At 115°E, there were local maxima of the original

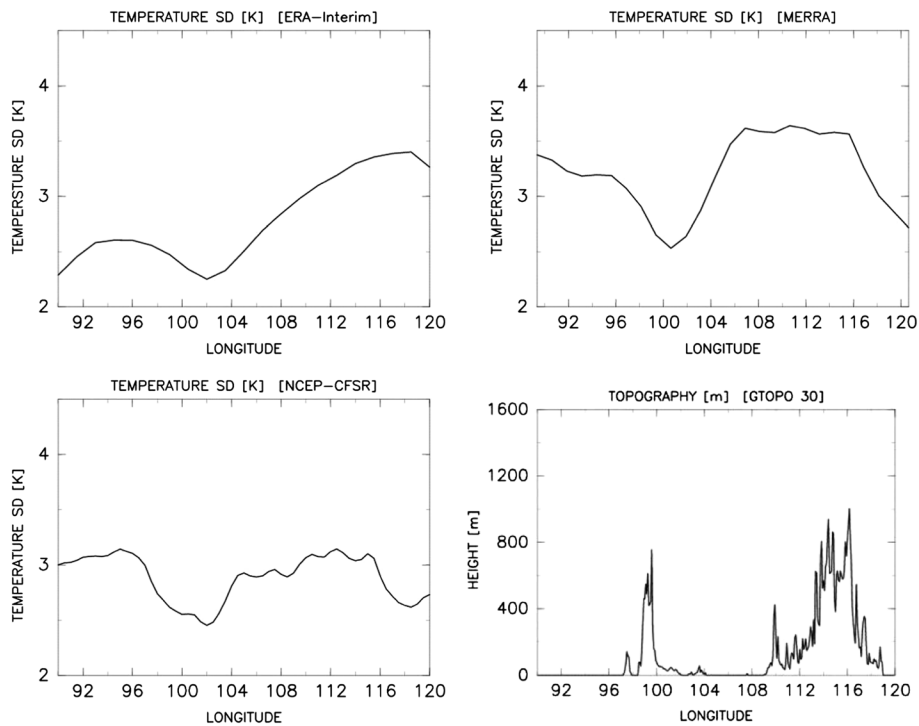


Figure 5. Longitudinal distribution of the standard deviation of temperature at 100 hPa for (a) ERA-Interim (1.5°N), (b) MERRA (1.875°N), and (c) NCEP-CFSR (1°N) during the period from 16 December 2006 to 15 January 2007. Horizontal resolutions are 1.5° , 1.25° , and 0.5° , respectively. (d) Longitudinal distribution of topography derived from GTOPO30 data. The height is averaged between 1°N and 2°N .

(5 day running mean) temperature on 1 December 2009, reaching $\sim 195\text{ K}$ (195 K), and on 20 December 2009, $\sim 199\text{ K}$ (195 K). Local minima of the original (5 day running mean) temperature were found on 15 December 2009, of $\sim 185\text{ K}$ (189 K), and on 25 December 2009, of $\sim 184\text{ K}$ (186 K). At 120°E , the local maxima of the original (5 day running mean) temperature were found on 2 December 2009, of $\sim 195\text{ K}$ (194 K), and on 22 December 2009, of $\sim 197\text{ K}$ (193 K). Local minima of the original (5 day running mean) temperature were $\sim 186\text{ K}$ (189 K) on 15 December 2009 and $\sim 186\text{ K}$ (187 K) on 25 December 2009. The period of these waves is about 10 days and is within the typical range of Kelvin waves. We also found that the amplitude of the temperature variation at 115°E (over the mountainous region) was $\sim 1\text{--}2\text{ K}$ higher than at 120°E . Similar higher (lower) temperature amplitudes were also found at 100°E (90°E , over the ocean) (not shown). Figures 6d and 6e show the power spectral densities of temperature at 115°E and 120°E , respectively. There is a clear difference in the power at periods between 8 and 12 days. We found that the temperature variations associated with Kelvin waves were different over the mountainous region and over the plain or the ocean.

3.3. Numerically Simulated Data (MJO Experiment)

Figure 7 shows the temperature variations simulated by the NICAM MJO experiment at four locations along 1.3°N at a height of 16.9 km, which is close to the average height of the tropopause: (a) 90°E over the ocean, (b) 100°E and (c) 115°E over the mountainous region, and (d) 120°E over the plain. As described in section 2, this experiment captured the eastward propagation of the convective system associated with the MJO whose horizontal scale is $\sim 6000\text{ km}$. The phase speed of the MJO is $\sim 3\text{ m s}^{-1}$, which is the typical propagation speed of the MJO [Madden and Julian, 1994]. The TTL temperature variations are mainly caused by Kelvin waves generated by convection associated with the MJO [Kubokawa et al., 2012]. We found that the temperature at all four locations is modulated by a signal with wave-number-one structure. This temperature variation is associated with Kelvin waves [Kubokawa et al., 2012]. At 90°E , the temperature is $\sim 192\text{ K}$ on 16 December 2006 (the first day of the simulation) and decreases with time to $\sim 188\text{ K}$ on 28 December 2006. After that, the temperature increases and reaches $\sim 200\text{ K}$ on 5 January 2007. At 100°E , the temperature is $\sim 200\text{ K}$ on 16 December 2006 and then decreases, reaching a minimum of $\sim 180\text{ K}$ on 30 December 2006.

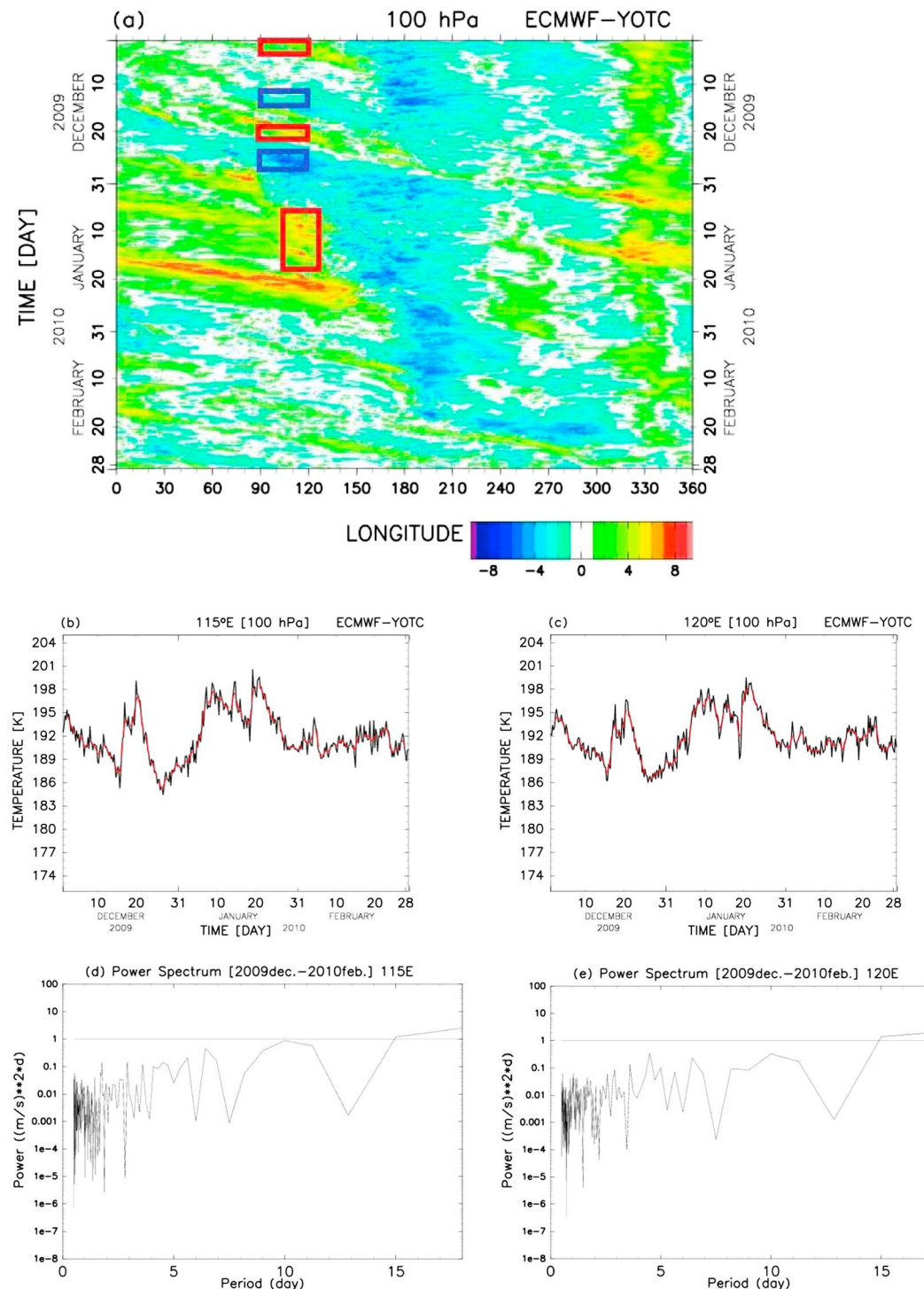


Figure 6. Temperature variations in high-resolution ECMWF-YOTC data. (a) Longitude-time distribution of the temperature anomaly at 100 hPa, averaged between 5°S and 5°N. The anomaly is with respect to the average value between 0° and 360°, and for the model integration period (1 December 2009 to 28 February 2010). The colored rectangles in Figure 6a indicate the data and longitudes discussed in the text. (b) Temperature variation at 115°E, 1.25°N around the tropopause (100 hPa). (c) Same as Figure 6b but for 120°E, 1.25°N. The red curves in Figures 6b and 6c indicate 5 day running means. (d) Power spectral density of temperature at 115°E. (e) Same as Figure 6d but for 120°E. The horizontal lines (power = 1) in Figures 6d and 6e are provided to enable a comparison of the spectral power density.

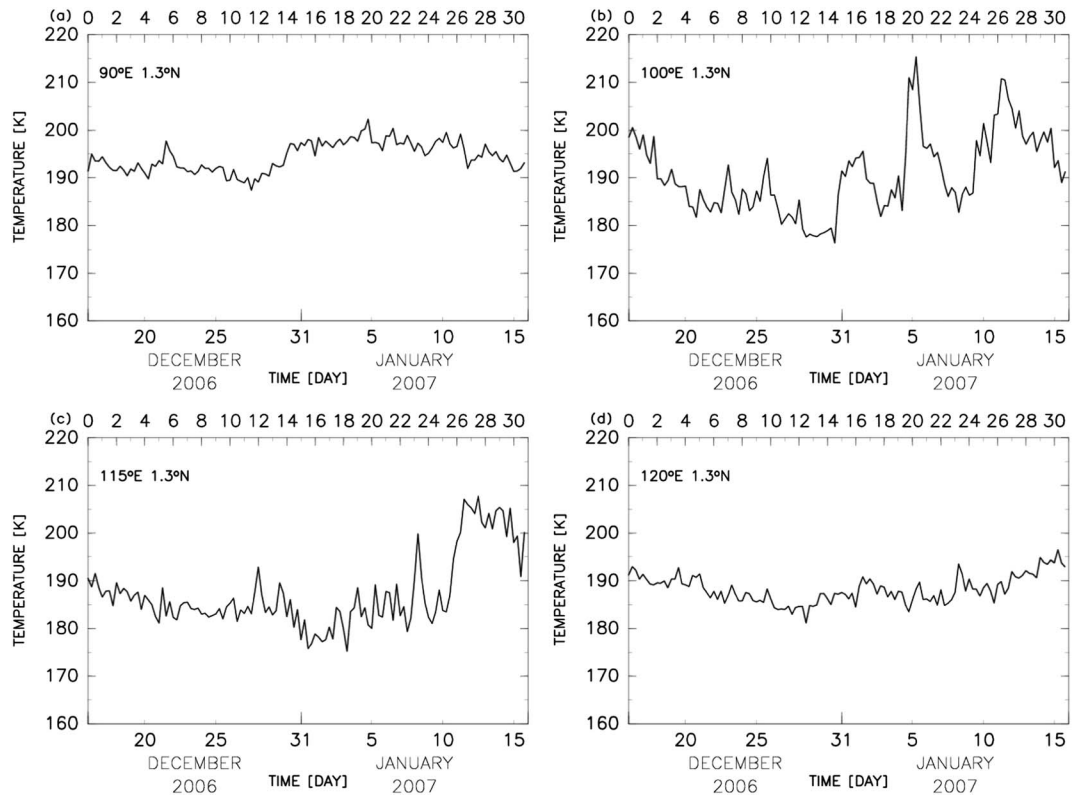


Figure 7. Temperature variation near the tropopause (16.9 km) at (a) 90°E, (b) 100°E, (c) 115°E, and (d) 120°E, from the NICAM MJO experiment. Latitude is set at 1.3°N.

The temperature then increases with time to a maximum of 210 K on 12 January 2007, before decreasing again. The temperature variation at this point implies the existence of a shorter time scale disturbance (about a 4 day period, which might be a mixed Rossby-gravity wave [Numaguti *et al.*, 1995]). At 115°E, the temperature was ~190 K on 16 December 2006 and decreased to a minimum of 175 K on 31 December 2006. The temperature then increased to a maximum of ~205 K on 12 January 2007. At 120°E, the temperature on 16 December 2006 was ~192 K. It then decreased to a minimum of ~185 K on 28 December 2006, before slowly increasing to ~195 K on 16 January 2007 (the last day of the simulation). At this location, the temperature had a local maximum (minimum) on 2 January 2007 (4 January 2007).

We found that the local minimum of temperature on 2 January 2007 corresponded to the cold phase of the wave-number-one Kelvin wave. The amplitudes of the temperature variations at 90°E, 100°E, 115°E, and 120°E were ~10 K, 20 K, 15 K, and 10 K, respectively. We found that the temperature variability was larger over the mountainous region (100°E and 115°E) than over the ocean and the plain (90°E and 120°E). In general, the amplitude of Kelvin waves is ~4–10 K [Fujiwara *et al.*, 1998; Yamamoto *et al.*, 2007]. In this simulation, the amplitude of Kelvin waves over the ocean and plain is ~10 K, which is consistent with the observed values. However, over the mountainous region the amplitude of the Kelvin waves exceeds 15 K, which is too large compared with the previously observed values. We found that such a large temperature variation over this region is not directly related to deep convection (not shown) and that there was no deep convection over the mountainous region when large temperature variations occurred, suggesting a possible influence of topography. An amplitude of 15 K is so large that it might result in the coldest temperature in the TTL. This might lead to strong local dehydration if such a large amplitude exists in the real atmosphere.

In summary, we investigated the temperature variations around the tropopause in regions located near and away from the mountainous region. In local radiosonde data, temperature variations near the mountainous region become ~1–2 K larger than in regions farther away. Note, however, that this difference is not always seen. In addition, there is a similar temperature change in the R/V *Roger Revelle* data. These large temperature changes are mainly observed when an MJO passes over the observatory. This may be caused by small-scale

Table 2. Experimental Design Used in the Stretch-NICAM^a

	Number of Vertical Levels	Height of Mountain	Vertical Grid Scheme
Control (Ctl)	40	default	default (terrain-following)
Experiment 1 (ExpL)	default	half	
Experiment 2 (ExpH)		double	
Experiment 3 (ExphyL)	default	default	hybrid e_fold = 10,000
Experiment 4 (ExphyH)			hybrid e_fold = 12,000

^aThe differences in settings with respect to the control experiment are shown in bold.

disturbances superimposed on the large and slow-moving temperature change associated with the MJO. Similarly, the data collected from the R/V *Roger Revelle* show small-scale disturbances superimposed on the large, slow temperature change. In the satellite data, temperature variations near the mountainous region are also large. The difference reached 2–5 K and was larger than that of the radiosonde data. This may be caused by the sparse sampling within the COSMIC data sets. In the reanalysis data, we found that the standard deviations of temperature near the mountainous region became larger with higher horizontal resolution of the reanalysis data set. In the ECMWF-YOTC data, the temperature amplitudes associated with Kelvin waves become larger over the mountainous region, reaching 1–2 K, consistent with the radiosonde observations. The temperature variations of the MJO experiment show larger amplitudes over the mountainous region (i.e., twice those over the ocean). Over the ocean, the amplitude is consistent with previous observations of the influence of Kelvin waves on the temperature at the tropical tropopause. We speculate that the amplitude difference between the mountainous region and the ocean is limited to ~2 K and that such a difference may be caused by gravity waves generated by the topography. In the next section, we investigate the reason for the difference between the observations and NICAM data.

4. Mechanism of Temperature Variation Near the Mountain Region

4.1. Sensitivity to Mountain Heights

In this section, we investigate the following three points by using the Stretch-NICAM [Tomita, 2008b]: (1) the influence of mountain heights on the temperature variations around the tropopause, (2) the effect of model configuration (vertical coordinate) on the temperature variations around the tropopause, and (3) the mechanism of temperature variations near the mountain region.

NICAM can be used as a regional model by transforming its grid mesh to focus on a specific region [Tomita, 2008b]. The Stretch-NICAM saves computational resources by focusing on a specific region at high resolution. The horizontal resolution becomes coarser for the region outside the target region, but in this study we are only interested in the local results within the target region. Because the Stretch-NICAM has the same dynamical core and physical package as the global-NICAM, it can be assumed that the model bias is the same in the two models.

First, we investigate the influence of mountain heights. Here we perform three experiments: control, experiment 1, and experiment 2 (hereafter referred to Ctl, ExpL, and ExpH, respectively). In ExpL and ExpH, we change the mountain height. Details of the experimental design are given in Table 2. For the initial conditions, we used data from the National Center for Environmental Prediction Global Data Assimilation System [National Centers for Environmental Prediction, 2011], and the integration was performed for 5 days, starting at 00:00 UTC on 1 June 2012. No nudging of the atmospheric observations was used during the integration. Sea surface temperature was kept constant. In this study, we discard the data on the first day because it is regarded as a spin-up phase and use the remaining 4 days of data for analysis. The output interval is 30 min. The microphysics scheme used in this study is NICAM Single-moment Water 6 [Tomita, 2008a], including water vapor, cloud water, rain, cloud ice, snow, and graupel as hydrometeors. The target area is over the tropical western Pacific, 20°S–20°N, 80°E–120°E, including the Indonesian Maritime Continent. We set the ratio of maximum/minimum horizontal grid size (stretching factor) as 100. The minimum horizontal grid spacing is ~7 km in the target area. GTOPO30 data were used as the topography, as presented in section 2. In this simulation, we used 40 vertical levels. The vertical grid interval is ~1.4 km around the tropopause, and the model top height was set at 40 km. For ExpL and ExpH, we changed the height of the

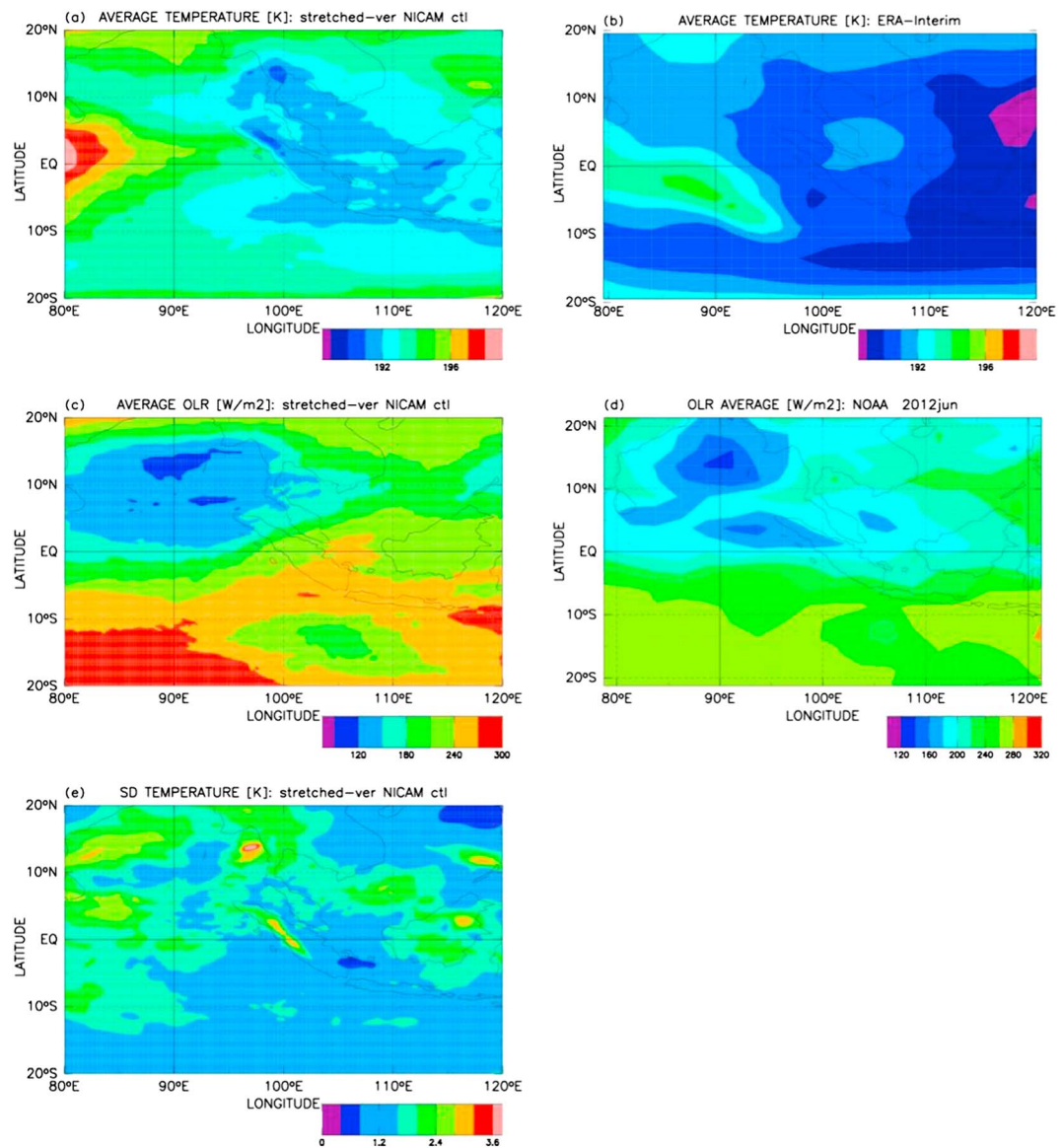


Figure 8. Horizontal distribution of averaged temperature during 2–5 June 2012 derived from (a) NICAM simulation (Ctl; see the text) at 16.9 km and (b) ERA-Interim data at 100 hPa. (c) Same as Figure 8a but for OLR. (d) Same as Figure 8c but derived from NOAA OLR data. (e) Horizontal distribution of the standard deviation of temperature near the tropopause derived from NICAM simulation (Ctl).

mountains in the target area; the mountain height is halved for ExpL and is doubled for ExpH. The areal averaged (20°S – 20°N , 80°E – 120°E) tropopause height is found to be 16.9 km in all three experiments.

Figures 8a and 8b show the time-averaged temperatures between 2 June and 5 June 2012 for the Ctl simulation and the ERA-Interim and NOAA OLR, respectively. At this time, an eastward propagating cold region near the tropopause passed over the Indonesian Maritime Continent (not shown), followed by a warm region. In Ctl, a time-averaged cold region is found over the Indonesian Maritime Continent. The location of the cold region in the simulation agrees fairly well with that of ERA-Interim. The warm region is also well simulated on the west side of the cold region; however, the simulated temperature has a warmer bias compared with ERA-Interim. Fujiwara et al. [2012] showed that ERA-Interim has a cold bias compared with other reanalysis data sets. Figures 8c and 8d also show the time-averaged OLR. Convective regions are found over the northwest side of Sumatra in both the simulation and the observations (NOAA OLR; Figure 8d). Figure 8e shows the standard deviations of temperature around the

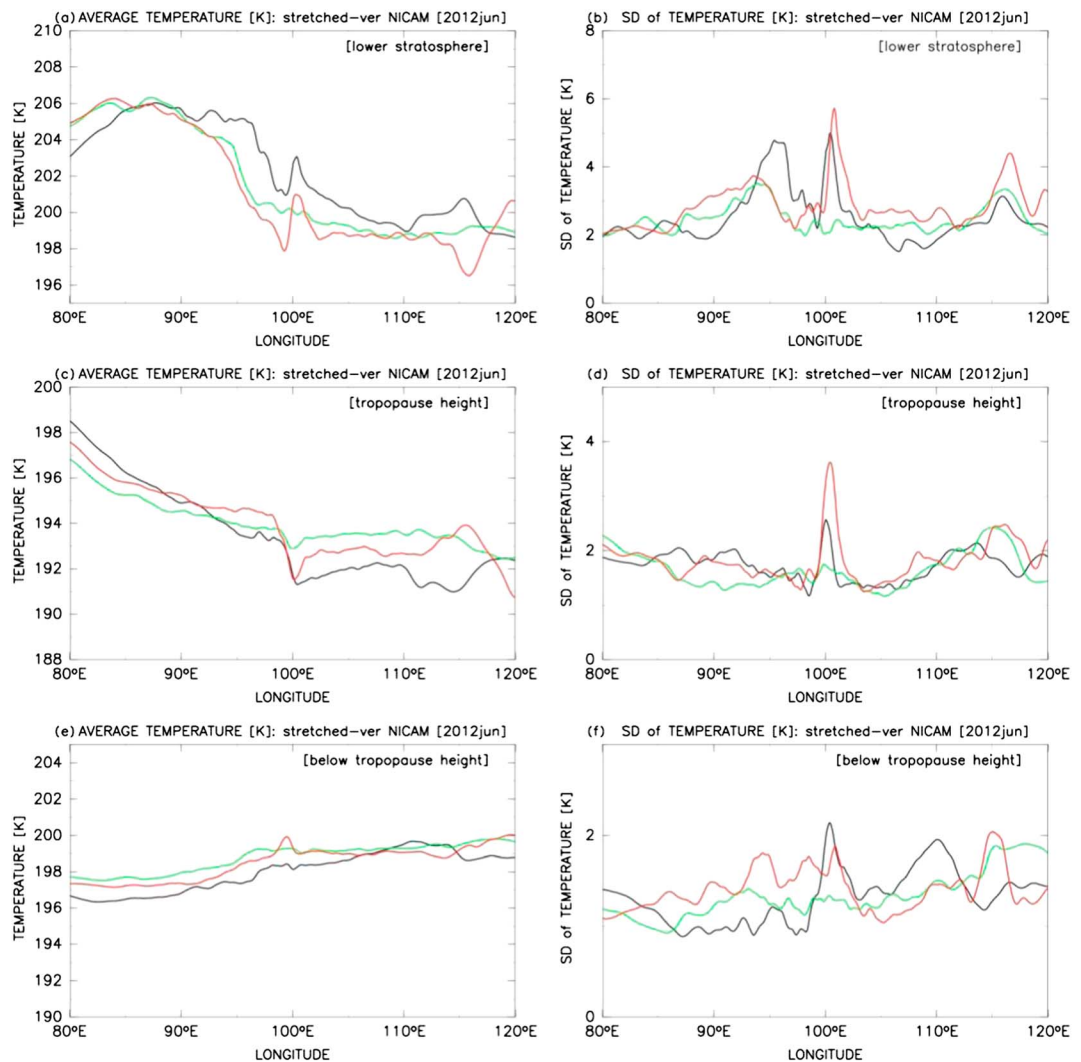


Figure 9. Longitudinal distribution of time-averaged temperature at 0.75°N at (a) 18.4 km, (c) 16.9 km, and (e) 15.5 km during 2–5 June 2012. Longitudinal distribution of standard deviation of temperature at (b) 18.4 km, (d) 16.9 km, and (f) 15.5 km during 2–5 June 2012. The black, green, and red lines are derived from Ctl, Expl, and ExpH, respectively (see the text).

tropopause for the simulation. Higher values of the standard deviation are seen over the mountains in Sumatra (equator, 100°E) and Kalimantan (4°N , 117°E).

Figure 9 shows the longitudinal distributions of the time-averaged temperature at 0.75°N (Figures 9a, 9c, and 9e) and the standard deviations of temperature in the upper troposphere and lower stratosphere (UTLS) region (Figures 9b, 9d, and 9f) at the same latitude. Near the tropopause level (16.9 km; Figure 9c), the averaged temperature has a minimum at around 100°E in all the experiments, although the temperature change is relatively small in Expl. Around 115°E , the averaged temperature becomes lower in Ctl, while it becomes warmer in ExpH. At around 18.4 km height in the lower stratosphere (Figure 9a), these local changes are reversed. Below the tropopause height at around 15.5 km (Figure 9e), the local temperature change around 100°E is found only in ExpH, but this change is smaller than that in Figure 9c (16.9 km, near the tropopause) and Figure 9a (18.4 km, in the lower stratosphere). The standard deviations of temperature near the tropopause (Figure 9d) have higher values near 100°E in Ctl and ExpH, but only increase slightly here in Expl. At around 115°E , high values are found in ExpH and Expl. Figure 9b (18.4 km, in the lower stratosphere) shows higher values of the standard deviation around 95°E , 100°E , and 115°E . At 100°E , higher values are found in Ctl and ExpH, while in the same plot, higher values are found in all experiments at around 95°E .

Thus, the temperature variability at 95°E does not depend on mountain heights. At 95°E the standard deviations of OLR are larger (not shown), indicating that the higher variabilities in temperature in this region are caused by convective activities. At 115°E, higher values are found for ExpL and ExpH, while there is no significant peak in Ctl. Below the tropopause height (Figure 9f), higher values are found at around 100°E for Ctl and ExpH. At around 100°E, there is no significant change for ExpL, while at 95°E and 115°E, the temperature variability increases with mountain height.

In summary, we performed experiments on sensitivity to mountain heights and found the following results: (1) the averaged tropopause temperature (at 16.9 km; Figure 9c) has a local minimum at around 100°E in all three experiments; (2) when the mountain height is doubled, a clear temperature variation is found in the UTLS region and the standard deviation doubles; and (3) when the mountain height is halved, the influence of topography on the temperature variability becomes very small at 100°E for the UTLS.

4.2. Choice of Vertical Coordinates

In the simulations Ctl, ExpL, and ExpH, a terrain-following vertical coordinate was used. Although this vertical coordinate is commonly used in many nonhydrostatic models, it is recognized that errors in horizontal pressure gradients may be produced over steep mountainous regions with this coordinate [Klemp, 2011]. Here we change the vertical coordinate system from the terrain-following coordinate to a hybrid coordinate, to examine whether spurious disturbances were generated [Simmons and Burridge, 1981]. We briefly explain the hybrid ζ coordinate system. The height $z(x, y, \zeta)$ in this system is $z = (z_t - Ah)\frac{\zeta}{z_t} + Ah$, where z_t is the top height of the model, $h(x, y)$ is the surface height distribution, and A is a constant. When $A = 1$, this is equivalent to the terrain-following coordinate system. For example, $z = \zeta$ at $h = 0$, while $z > \zeta$ at $h > 0$; in other words, the height of a ζ surface over a mountain is higher than that over the ocean. This produces artificial horizontal pressure gradients even on the same ζ surface. When A is closer to zero, the artificial horizontal gradient becomes closer to zero. According to Klemp [2011], the parameter A can be specified to transition the vertical coordinate from the terrain-following at the surface toward constant height surfaces aloft more rapidly than in the terrain-following coordinate. The hybrid coordinate is known to reduce errors in pressure gradients above a fixed level (e-folding height, m). We performed two experiments with e-folding heights of 10,000 m (ExphyL) and 12,000 m (ExphyH).

Figure 10 shows the longitudinal distributions of average temperature and the standard deviation of temperature in the UTLS region for Ctl, ExphyL, and ExphyH. The peak in the average temperature around 100°E and 115°E is reduced in ExphyL and ExphyH near the tropopause (16.9 km; Figure 10b) and in the lower stratosphere (18.4 km; Figure 10a). Similar to the average temperature, the standard deviation of temperature is reduced in ExphyL and ExphyH around (1) 95°E, 100°E, and 115°E in the lower stratosphere (Figure 10b), (2) 100°E and 115°E near the tropopause (Figure 10d), and (3) 100°E below the tropopause (Figure 10f).

It is clear that the errors in pressure gradients around the mountainous region were produced by the use of the terrain-following coordinate, as is the high standard deviation of temperature simulated by the MJO experiment shown in Figure 7. However, there are still slightly higher values (~ 0.5 K) of the standard deviation around 100°E near the tropopause when the hybrid coordinate is used in ExphyL and ExphyH (Figure 10d). In the next section, we use the results from ExphyH and discuss the local temperature variation over the mountainous region to investigate its cause.

4.3. Analysis of Data From the Hybrid Coordinate Simulation

Figure 11 shows the horizontal distributions of the anomaly fields of temperature and meridional wind obtained by applying a spatial band-pass filter of 0.4°–6.0°. We applied the filter to show the characteristics of gravity waves more clearly. In Figures 11a and 11b, the temperature and wind anomaly fields have a clear wave pattern along the dashed lines. At this time, there is a warm region running from northwest to southeast, with cold regions on either side. In the lower stratosphere (Figure 11b), the phase of this wave pattern is reversed. The wave patterns in temperature and meridional wind anomalies show a quadratic phase difference along the dashed lines. This phase relationship indicates that the disturbances are gravity waves with a horizontal wavelength of 200 km and a temperature (meridional wind) amplitude of ~ 2 K (2 m s^{-1}). Figure 11c shows the horizontal-vertical distribution of temperature and meridional wind anomalies from the lower troposphere to the lower stratosphere. Here we find the wave structure extending from the lower

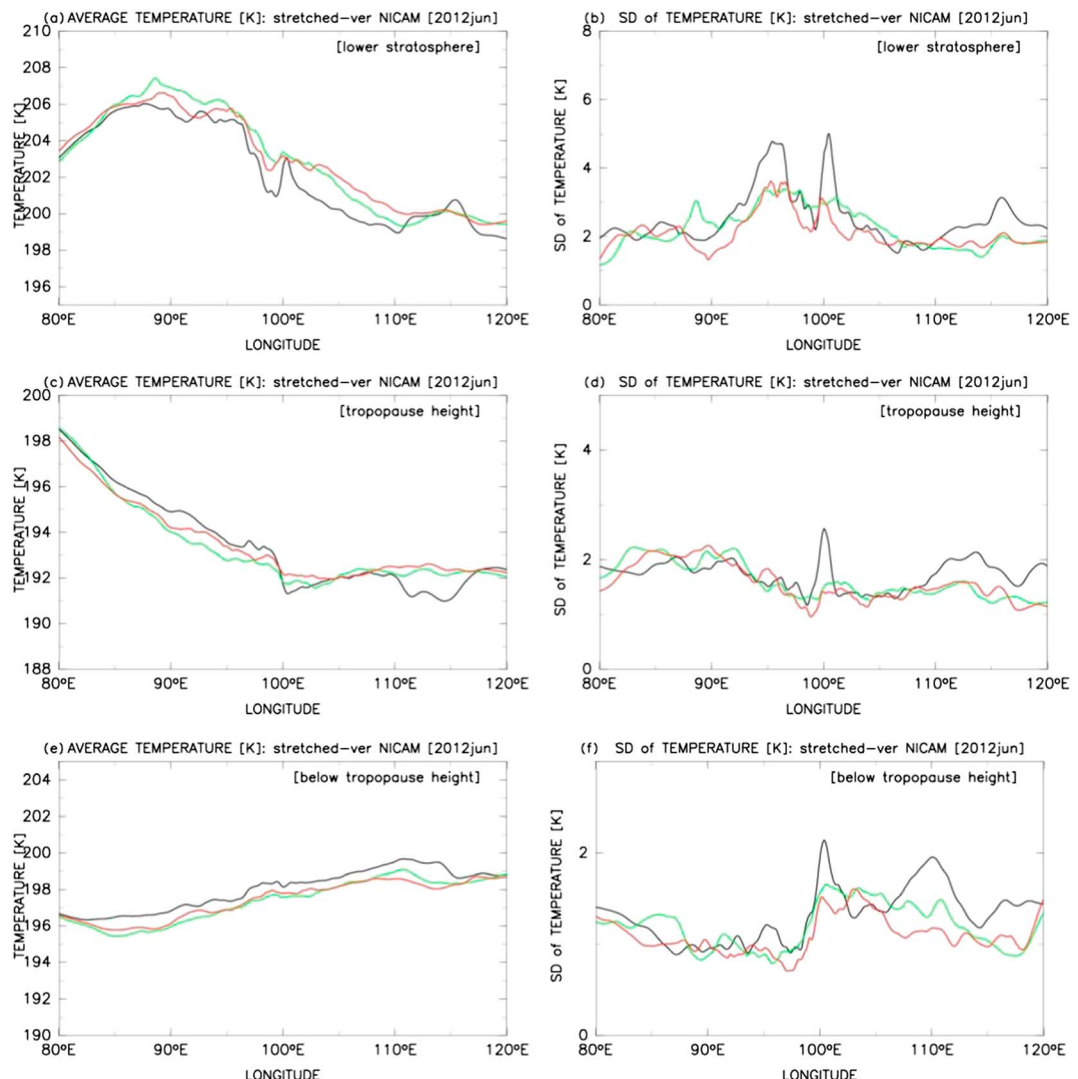


Figure 10. Longitudinal distribution of time-averaged temperature at 0.75°N at (a) 18.4 km , (c) 16.9 km , and (e) 15.5 km during 2–5 June 2012. Longitudinal distribution of standard deviation of temperature at (b) 18.4 km , (d) 16.9 km , and (f) 15.5 km during 2–5 June 2012. The black, green, and red lines are derived from Ctl, ExphyL, and ExphyH, respectively.

troposphere to the lower stratosphere. This wave structure originates at a height of 1 km (the vertical axis starts from 1.0 km). Because the mountain height in this region is $\sim 1\text{ km}$, this wave is likely generated by a mountain in the Indonesian Maritime Continent. The vertical wavelength is $\sim 5\text{ km}$. According to linear wave theory, we estimate the period of this wave to be $\sim 7\text{ h}$.

When a Kelvin wave with a large temperature amplitude passes over the Indonesian Maritime Continent (see Figure 8a), gravity waves are generated by the mountains and are superimposed on the Kelvin wave around the height of the tropopause (see Figure 11a). This superposition of the waves produces the large temperature variation around the tropopause (Figure 10d). The mountainous region in the Indonesian Maritime Continent ($\sim 100^{\circ}\text{E}$) is a favorable area for the superposition of gravity waves onto Kelvin waves.

5. Concluding Remarks

We investigated temperature variations in the TTL over the mountain region by using various observational data sets including radiosonde data, satellite data, and reanalysis data at different horizontal resolutions, together with numerical data simulated by NICAM.

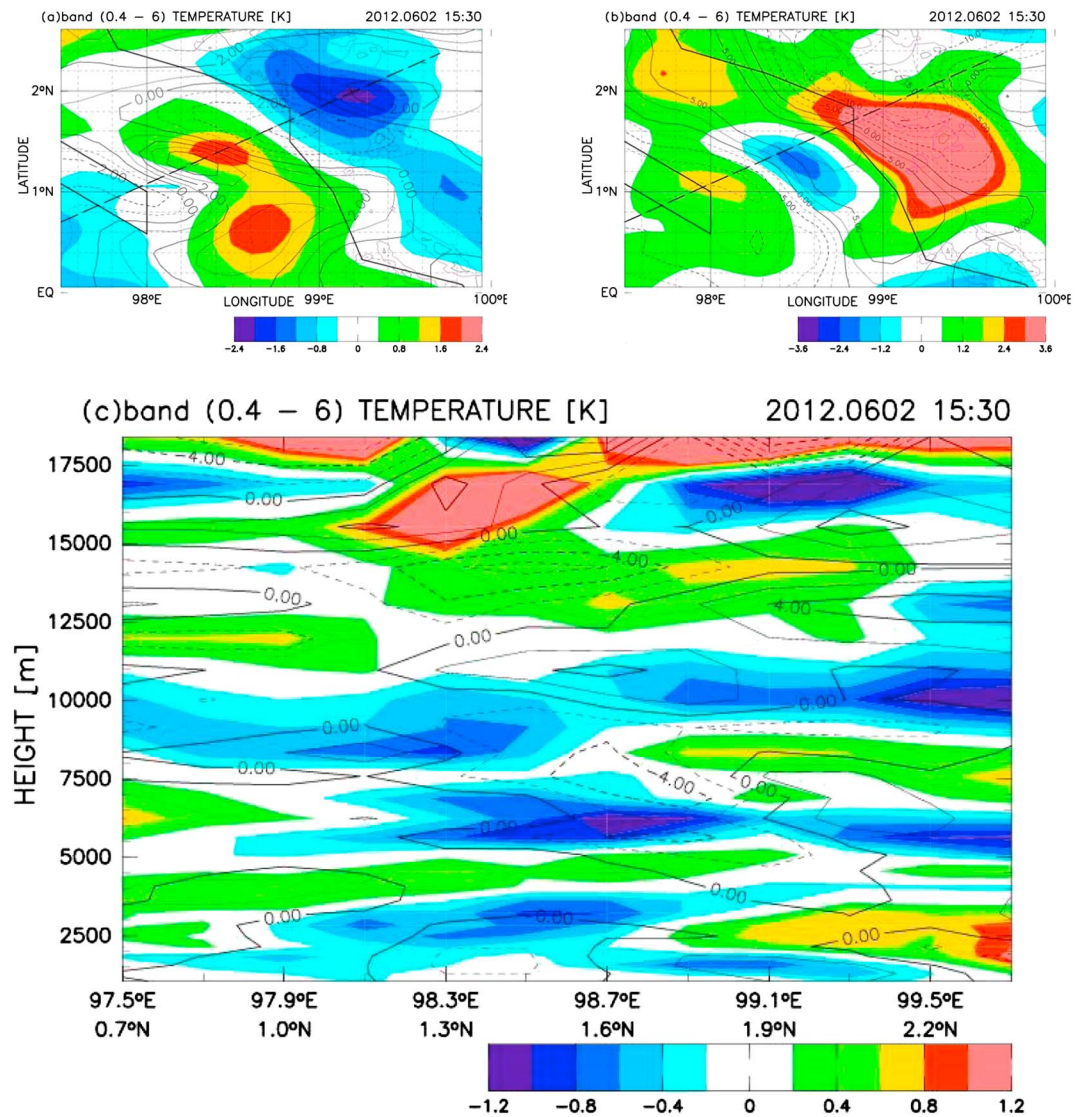


Figure 11. Horizontal distributions of temperature (color shading) and meridional wind anomaly (contours) at (a) 16.9 km and (b) 18.4 km at 15:30 LT on 2 June 2012. A band-pass filter of 0.4°–6.0° has been applied. The slanted dashed lines in Figures 11a and 11b run from (97.5°E, 0.7°N) to (99.7°E, 2.4°N). The thick lines indicate the border of countries. The thick contours indicate the 1500 m topography. (c) Horizontal-vertical distribution of temperature and meridional wind anomalies from the lower troposphere to the lower stratosphere (1.0–18.5 km) at 15:30 LT on 2 June 2012. The horizontal axis corresponds to the thick dashed lines in Figures 11a and 11b.

We examined the variations in tropopause temperature by using radiosonde data obtained during the CINDY/DYNAMO observational campaign. We selected data from the observatories around 100°E to represent the mountainous region, and those around 120°E to represent the plain. Radiosonde data at Male (90°E, over the island) and from the observing ship R/V *Roger Revelle* were also used. We found that when Kelvin waves with a larger temperature amplitude pass over the western Pacific region, temperature variations near the observatories located around 100°E (mountains) become larger than those located around 120°E (plains) and at Male. The difference in amplitude between these two regions reaches 1–2 K. In contrast, the temperature variation derived from the data obtained from the R/V *Roger Revelle* is similar to that near 100°E. These larger temperature variations are produced by the superposition of waves of different scales.

We investigated the temperature variations during the rainy season using COSMIC satellite data between 2006 and 2010. Because of the limitations of data coverage, we calculate the standard deviations around

the tropopause. We found higher values of the standard deviation, 5–8 K, over the mountainous region, while the average value of the standard deviation for 90°E and 120°E is ~3.2 K.

Using the reanalysis data with different horizontal resolutions, we found that the greater temperature variation over the mountainous region becomes clearer when increasing the horizontal resolution of the reanalysis data. In the ECMWF-YOTC data with the highest horizontal resolution, temperature variations associated with the Kelvin waves over the mountainous region are ~1–2 K larger than over the plain. The power spectrum of Kelvin waves shows that the power in the 8–12 day period range over the mountainous region is stronger than that over the plain. The results from these reanalysis data indicate that temperature variations associated with Kelvin waves are larger over the mountainous region.

In the MJO experiment, simulated by the global-NICAM with a horizontal mesh interval of 7 km, when the Kelvin waves pass over the Indonesian Maritime Continent the temperature amplitude over the mountainous region is twice that over the plains. Note that the amplitude over the ocean is consistent with observations, while the temperature variations over the mountainous region derived from the MJO experiment are much larger than in the observations. To investigate this difference, we performed sensitivity experiments by using the Stretch-NICAM, which is computationally less expensive than the global-NICAM. When the mountain height is doubled (halved), the average temperature at tropopause height increases (decreases) over the mountain region, and the standard deviation of temperature increases (decreases). Thus, the mountain height greatly affects the temperature variations in the UTLS region.

We tested the dependency on the choice of the vertical coordinate by changing from the terrain-following coordinate to a hybrid coordinate with two different e-folding height scales. The temperature variations and standard deviation over the mountain region become smaller and more realistic when the hybrid coordinate is used. However, even when the hybrid coordinate is used, the standard deviation is appreciably higher over the mountainous region around 100°E (0.5 K, smaller than the radiosonde observations), and this increase is robust. By analyzing the results of the simulation with the hybrid coordinate, we found that this high standard deviation is caused by gravity waves generated by the mountains in the Indonesia Maritime Continent (~100°E).

There are two important results from this study. First, we found large temperature variations over the mountainous region over the Indonesian Maritime Continent. The variations, ~1–2 K over the mountainous region, are associated with Kelvin waves passing over the Indonesia Maritime Continent. The magnitude of this variation is about the same as that of the seasonal cycle of tropopause temperature. The mountainous region can be considered as a source of gravity waves, and various waves (from small to large scales) coexist over the mountainous region. We propose that a superposition of gravity waves and a Kelvin wave produces the large temperature variations. According to the quasi-horizontal transport theory proposed by Holton and Gettelman [2001], the minimum temperature is important for dehydration. When an air mass passes over the mountain region, it may experience a much larger horizontal temperature gradient. This may affect the amount of water vapor entering the stratosphere. The second point is concerned with the model configuration. The terrain-following coordinate system generally used for atmospheric models may produce larger temperature variations near the tropopause over mountainous regions. The choice of vertical coordinate needs to be considered carefully if we wish to discuss temperature variations near the tropopause and dehydration. We found some discrepancy between radiosonde data and reanalysis data. In the ECMWF-YOTC data, the amplitude of Kelvin waves becomes larger; however, the temperature variations associated with the Kelvin waves are not caused by the superposition of the waves (Kelvin waves and gravity waves). In addition, at 100°E in the reanalysis data the standard deviation is not high. These differences have yet to be resolved. In a future work, we will investigate the relationship between the phase of Kelvin waves and the influence of the location of mountains in generating gravity waves.

Acknowledgments

We thank Hirofumi Tomita and other researchers responsible for the development of the NICAM. We thank Noriyuki Nishi for invaluable comments and discussions on this manuscript. We used the Interpolated OLR data provided by NOAA/OAR/ESRL PSD, Boulder, Colorado, USA, from their website at <http://www.esrl.noaa.gov/psd/>, along with the NCEP/NCAR Reanalysis data set and the NCEP CFSR data set. The ERA-Interim data set and ECMWF-YOTC data set were obtained from the ECMWF data server. MERRA was obtained from the Goddard Earth Sciences Data and Information Services Center, Greenbelt, Maryland, from their website (<http://disc.sci.gsfc.nasa.gov/mdi/>). We thank NSPO and UCAR for providing the COSMIC data or data products. The NICAM MJO experiments were performed by using the Earth Simulator housed at the Japan Agency for Marine-Earth Science and Technology. Figures 1–11 were produced by using the GFD-DENNOU Library.

References

- Anthes, R. A., et al. (2008), The COSMIC/FORMOSAT3 Mission: Early results, *Bull. Am. Meteorol. Soc.*, 89, 313–333.
Dee, D., et al. (2011), The ERA-Interim reanalysis: Configuration and performance of the data assimilation system, *Q. J. R. Meteorol. Soc.*, 137, 553–597, doi:10.1002/QJ.828.
Fueglistaler, S. A., E. Dessler, T. J. Dunkerton, L. Folkins, Q. Fu, and P. W. Mote (2009), Tropical tropopause layer, *Rev. Geophys.*, 47, RG1004, doi:10.1029/2008RG000267.

- Fujiwara, M., K. Kita, and T. Ogawa (1998), Stratosphere–troposphere exchange of ozone associated with the equatorial Kelvin waves as observed with ozonesondes and rawinsondes, *J. Geophys. Res.*, 103(D15), 19,173–19,182, doi:10.1029/98JD01419.
- Fujiwara, M., et al. (2010), Seasonal to decadal variations of water vapor in the tropical lower stratosphere observed with balloon-borne cryogenic frostpoint hygrometers, *J. Geophys. Res.*, 115, D18304, doi:10.1029/2010JD014179.
- Fujiwara, M., J. Suzuki, A. Gettelman, M. I. Hegglin, H. Akiyoshi, and K. Shibata (2012), Wave activity in the tropical tropopause layer in seven reanalysis and four chemistry climate model data sets, *J. Geophys. Res.*, 117, D12105, doi:10.1029/2011JD016808.
- Highwood, E. J., and B. J. Hoskins (1998), The tropical tropopause, *Q. J. R. Meteorol. Soc.*, 124, 1579–1604.
- Holton, J. R., and A. Gettelman (2001), Horizontal transport and the dehydration of the stratosphere, *Geophys. Res. Lett.*, 28(14), 2799–2802, doi:10.1029/2001GL013148.
- Holton, J. R., P. H. Haynes, M. E. McIntyre, A. R. Douglass, R. B. Rood, and L. Pfister (1995), Stratosphere-troposphere exchange, *Rev. Geophys.*, 33, 403–440, doi:10.1029/95RG02097.
- Immler, F., K. Kruger, M. Fujiwara, G. Verver, M. Rex, and O. Schrems (2008), Correlation between equatorial Kelvin waves and the occurrence of extremely thin ice clouds at the tropical tropopause, *Atmos. Chem. Phys.*, 8, 4019–4026.
- Inai, Y., F. Hasebe, M. Fujiwara, M. Shiotani, N. Nishi, S.-Y. Ogino, H. Vömel, S. Iwasaki, and T. Shibata (2013), Dehydration in the tropical tropopause layer estimated from the water vapor match, *Atmos. Chem. Phys.*, 13, 8623–6642, doi:10.5194/acp-13-8623-2013.
- Klemp, J. B. (2011), A terrain-following coordinate with smoothed coordinate surfaces, *Mon. Weather Rev.*, 139, 2163–2169.
- Kley, D. J., J. M. Russell, and C. Philips (Eds) (2000), *SPARC assessment of upper tropospheric and stratospheric water vapor*, WCRP, vol. 113, 312 pp., World Meteorol. Organ., Geneva, Switzerland.
- Kubokawa, H., M. Fujiwara, T. Nasuno, and M. Satoh (2010), Analysis of the tropical tropopause layer using the Nonhydrostatic Icosahedral Atmospheric Model (NICAM): Aqua-planet experiments, *J. Geophys. Res.*, 115, D08102, doi:10.1029/2009JD012686.
- Kubokawa, H., M. Fujiwara, T. Nasuno, H. Miura, M. K. Yamamoto, and M. Satoh (2012), Analysis of the tropical tropopause layer using the Nonhydrostatic Icosahedral Atmospheric Model (NICAM): 2. An experiment under the atmospheric conditions of December 2006 to January 2007, *J. Geophys. Res.*, 117, D17114, doi:10.1029/2012JD017737.
- Madden, R. A., and P. R. Julian (1994), Observations of the 40–50-day tropical oscillation—A review, *Mon. Weather Rev.*, 122, 814–837.
- Miura, H., M. Satoh, T. Nasuno, A. T. Noda, and K. Oouchi (2007), A Madden-Julian Oscillation event realistically simulated by a global cloud-resolving model, *Science*, 318(5857), 1763–1765.
- Moncrieff, M. W., D. E. Waliser, M. J. Miller, M. A. Shapiro, G. R. Asrar, and J. Caughey (2012), Multiscale convective organization and the YOTC Virtual Field Campaign, *Bull. Am. Meteorol. Soc.*, 93(8), 1171–1187, doi:10.1175/BAMS-D-11-00233.1.
- Mote, P. W., K. H. Rosenlof, M. E. McIntyre, E. S. Carr, J. C. Gille, J. R. Holton, J. S. Kinnersley, H. C. Pumphrey, J. M. Russell III, and J. W. Waters (1996), An atmospheric tape recorder: The imprint of tropical tropopause temperatures on stratospheric water vapor, *J. Geophys. Res.*, 101, 3989–4006, doi:10.1029/95JD03422.
- NCEP (cited 2011), NCEP FNL operational model global tropospheric analyses, continuing from July 1999, Research Data Archive at the National Center for Atmospheric Research, Computational and Information Systems Laboratory, Boulder, Colo. [Available at <http://rda.ucar.edu/datasets/ds083.2>.]
- Newell, R. E., and S. Gould-Stewart (1981), A stratospheric fountain?, *J. Atmos. Sci.*, 38, 2789–2796.
- Nishimoto, E., and M. Shiotani (2012), Seasonal and interannual variability in the temperature structure around the tropical tropopause and its relationship with convective activities, *J. Geophys. Res.*, 117, D02104, doi:10.1029/2011JD016936.
- Numaguti, A., R. Oki, K. Nakamura, K. Tsuboki, N. Misawa, T. Asai, and Y. M. Kodama (1995), 4–5 day-period variation and low-level dry air observed in the equatorial Western Pacific during the TOGA-COARE IOP, *J. Meteorol. Soc. Jpn.*, 73(2B), 267–290.
- Parker, D. E. (1973), Equatorial Kelvin waves at 100 millibars, *Q. J. R. Meteorol. Soc.*, 99, 116–129.
- Pfister, L., K. R. Chan, T. P. Bui, S. Bowen, M. Legc, B. Gary, K. Kelly, M. Proffitt, and W. Starr (1993), Gravity waves generated by a tropical cyclone during the STEP tropical field program: A case study, *J. Geophys. Res.*, 98(D5), 8611–8638, doi:10.1029/92JD01679.
- Rienecker, M. M., et al. (2011), MERRA: NASA's Modern-Era Retrospective Analysis for Research and Applications, *J. Clim.*, 24, 3624–3648, doi:10.1175/JCLI-D-11-00015.1.
- Saha, S., et al. (2010), The NCEP Climate Forecast System Reanalysis, *Bull. Am. Meteorol. Soc.*, 91, 1015–1057, doi:10.1175/2010BAMS3001.1.
- Satoh, M., T. Matsuno, H. Tomita, H. Miura, T. Nasuno, and S. Iga (2008), Nonhydrostatic Icosahedral Atmospheric Model (NICAM) for global cloud resolving simulations, *J. Comput. Phys.*, 227, 3486–3514, doi:10.1016/j.jcp.2007.02.006.
- Satoh, M., et al. (2014), The Non-hydrostatic Icosahedral Atmospheric Model: Description and development, *Progr. Earth Planet. Sci.*, 1, 18, doi:10.1186/s40645-014-0018-1.
- Satomura, T. (1996), Supplement to "Numerical simulation of lee-wave events over the Pyrenees", *J. Meteorol. Soc. Jpn.*, 74, 147–153.
- Satomura, T., and P. Bougeault (1994), Numerical simulation of lee-wave events over the Pyrenees, *J. Meteorol. Soc. Jpn.*, 72, 173–195.
- Seidel, D. J., R. J. Ross, and J. K. Angell (2001), Climatological characteristics of the tropical tropopause as revealed by radiosondes, *J. Geophys. Res.*, 106(D8), 7857–7878, doi:10.1029/2000JD900837.
- Simmons, A. J., and D. M. Burridge (1981), An energy and angular-momentum conserving vertical finite-difference scheme and hybrid vertical coordinates, *Mon. Weather Rev.*, 109, 758–766.
- Suzuki, J., M. Fujiwara, T. Nishizawa, R. Shirooka, K. Yoneyama, M. Katsumata, I. Matsui, and N. Sugimoto (2013), The occurrence of cirrus clouds associated with eastward propagating equatorial $n = 0$ inertio-gravity and Kelvin waves in November 2011 during the CINDY2011/DYNAMO campaign, *J. Geophys. Res. Atmos.*, 118, 12,941–12,947, doi:10.1002/2013JD019960.
- Tomita, H. (2008a), New microphysical schemes with five and six categories by diagnostic generation of cloud ice, *J. Meteorol. Soc. Jpn.*, 86A, 121–142, doi:10.2151/jmsj.86A.121.
- Tomita, H. (2008b), A stretched icosahedral grid by a new grid transformation, *J. Meteorol. Soc. Jpn.*, 86A, 107–119, doi:10.2151/jmsj.86A.107.
- Tomita, H., and M. Satoh (2004), A new dynamical framework of nonhydrostatic global model using the icosahedral grid, *Fluid Dyn. Res.*, 34, 357–400.
- Tsuda, T., Y. Murayama, H. Wiryo Sumarto, S. Woro, B. Harijono, and S. Kato (1994), Radiosonde observations of equatorial atmosphere dynamics over Indonesia. 1. Equatorial waves and diurnal tides, *J. Geophys. Res.*, 99(D5), 10,491–10,505, doi:10.1029/94JD00355.
- Yamamoto, M. K., N. Nishi, T. Horinouchi, M. Niwano, and S. Fukao (2007), Vertical wind observation in the tropical upper troposphere by VHF wind profiler: A case study, *Radio Sci.*, 41, RS5002, doi:10.1029/2005RS003333.
- Yoneyama, K., C. Zhang, and C. N. Long (2013), Tracking pulses of the Madden-Julian oscillation, *Bull. Am. Meteorol. Soc.*, 94, 1871–1891.
- Zhang, S. D., F. Yi, C. M. Huang, K. M. Huang, Q. Gan, Y. H. Zhang, and Y. Gong (2013), Latitudinal and altitudinal variability of lower atmospheric inertial gravity waves revealed by U.S. radiosonde data, *J. Geophys. Res. Atmos.*, 118, 7750–7764.
- Zhang, S. D., C. M. Huang, K. M. Huang, F. Yi, Y. H. Zhang, Y. Gong, and Q. Gan (2014), Spatial and seasonal variability of medium- and high-frequency gravity waves in the lower atmosphere revealed by US radiosonde data, *Ann. Geophys.*, 32, 1129–1143.